Eur. Phys. J. E (2015) **38**: 23
DOI 10.1140/epje/i2015-15023-6

THE EUROPEAN PHYSICAL JOURNAL E

Regular Article

Topological binding and elastic interactions of microspheres and fibres in a nematic liquid crystal

M. Nikkhou[1], M. Škarabot[1], and I. Muševič[1,2,a]

[1] J. Stefan Institute, Jamova 39, SI-1000, Ljubljana, Slovenia
[2] Faculty of Mathematics and Physics, University of Ljubljana, Jadranska 19, SI-1000, Ljubljana, Slovenia

Received 23 December 2014 and Received in final form 13 February 2015
Published online: 30 March 2015 –

Abstract. We present a detailed analysis of topological binding and elastic interactions between a long, and micrometer-diameter fiber, and a microsphere in a homogeneously aligned nematic liquid crystal. Both objects are surface treated to produce strong perpendicular anchoring of the nematic liquid crystal. We use the opto-thermal micro-quench of the laser tweezers to produce topological defects with prescribed topological charge, such as pairs of a Saturn ring and an anti-ring, hyperbolic and radial hedgehogs on a fiber, as well as zero-charge loops. We study the entanglement and topological charge interaction between the topological defects of the fiber and sphere and we observe a huge variety of different entanglement topologies and defect-mediated elastic bindings. We explain all observed phenomena with simple topological rule: like topological charges repel each other and opposite topological charges attract. These binding mechanisms not only demonstrate the fascinating topology of nematic colloids, but also open a novel route to the assembly of very complex topological networks of fibers, spheres and other objects for applications in liquid crystal photonics.

1 Introduction

Liquid crystal (LC) colloids have attracted great attention in recent years as a novel composite soft matter system with interesting material properties [1–3]. Combination of particles and a LC gives rise to unique topological properties that can not be seen in conventional colloidal systems. The emergent topology of nematic colloids is due to the orientational order of LC and surface anchoring of LC molecules on closed surfaces of colloidal inclusions of various topological complexity. When a small particle is immersed in a uniformly oriented nematic, the LC molecules align around the particle in preferred direction with respect to the surface. Because it is not possible to fill the space between the particle and the far field uniformly, various topological defects are created, depending on the anchoring at the surface of colloidal particle and confinement. For instance, a spherical particle with normal surface anchoring immersed in a uniformly aligned nematic carries either point-like defect, called the hyperbolic hedgehog [3, 4], or it is encircled by a small defect loop, called *Saturn ring* [5–8]. A microsphere with planar surface alignment is accompanied by two surface defects, called boojums [3, 4].

Topological defects in nematic colloids give rise to several interesting properties, such as the strong force between colloidal particles, which is of elastic origin. These interactions are long range, anisotropic, and are responsible for self-assembling of nematic colloids or directed assembly, where interesting colloidal superstructures were designed and produced. The topology therefore makes the nature of pair interactions in LC colloids quite different compared to water-based colloids, where Coulomb and van der Waals interactions are dominant [9, 10].

The inter-particle interactions in the nematic liquid crystalline media are several orders of magnitude larger compared to the isotropic solvents. The long-range interaction between two colloidal particles far apart from each other depends on the orientation of the LC molecules in the vicinity of the particle, and is of a *dipolar* type, when the particle is accompanied by a hedgehog defect and *quadrupolar* when the particle carries Saturn ring or two boojum defects. Various types of self-assembled structures were observed such as linear [11–15] and kinked [16] chains of colloidal particles, colloidal clusters [4], particle-stablized gels [17], 2D and 3D colloidal crystals [15,16,18–25], self-assembled structure of micro-rods [26], and cellular structures [27–29].

Besides pair interactions due to the isolated topological point and loop defects, another mechanism of binding, called topological entanglement, was predicted [30,31] and observed [32]. In topological entanglement, two isolated Saturn rings are thermally fused together in a single loop, using localized heating with laser tweezers. The loop can

[a] e-mail: igor.musevic@ijs.si

show three different topological conformations and in all cases generates a string-like force between the two colloidal particles. Because of the anisotropy of the LC molecules, the nematic colloidal superstructures respond quite easily to external stimuli, such as an electric field [24,25]. Therefore, superstructures of LC colloids are easily tunable, and may thus serve as controllable photonic materials.

Nearly in parallel with the increased interest in self-assembly and topological properties of nematic colloids, liquid crystal micro-photonics has emerged as a relatively new direction in liquid crystal research [33]. It is based on a series of experiments, which demonstrated lasing [34], waveguiding [35] and resonant transport [36] of light using micro-photonic elements, such as microlasers, tunable optical microresonators [37], Whispering Gallery Mode microsensors [38], and microfibers, all of them made entirely of liquid crystals. These photonic microelements are actually self-assembled by mixing different liquid crystals with non-miscible carrier liquid, such as water, glycerol, PDMS etc. Because of chemical incompatibility, microdroplets and microfibers are spontaneously created in these liquid-liquid dispersions, which have various photonic functionalities. Now, in order to assemble these individual photonic microelements into functional photonic microcircuits, forces are needed that are able to connect and bind these microelements into some sort of functional photonic microcircuits, where the binding energy of individual microelement should exceed tens of k_BT and the gap between the surfaces should be below 100 nm. Structural forces in nematic colloids are a natural candidate for this purpose, and there are several possible topologically different colloidal binding mechanisms, as explained above.

The purpose of this work is to explore and demonstrate the topological binding of two most simple photonic micro-objects into a basic photonic microcircuit: a microsphere and a microfiber, both surface-functionalized to give perpendicular surface-anchoring of NLC. Both objects are topologically equivalent and are characterized by the genus $g = 0$ [39]. The article is organized as follows. We first discuss the laser tweezers creation of a series of pairs of a Saturn ring and Saturn anti-ring on a fibre, when the fiber is set parallel to the overall direction of the NLC (*i.e.* the rubbing direction). For a detailed discussion of this part of the work, the reader is directed to our recent publication, where all experimental details are thoroughly discussed [40]. Being able to produce an arbitrary number of oppositely charged topological monopoles, one can study pair-interaction forces and entanglement, which is in detail described and discussed further in this article. An even more interesting topology is discussed in sect. 3, where the fibre is set perpendicular to the rubbing direction. In this case a variety of new phenomena is observed, including zero-topological charge loops, and the interactions and entanglement with spherical colloids are described and discussed. The work concludes with the announcement of even more interesting topological phenomena observed when the fiber and the microspheres are immersed in chiral nematic liquid crystal.

2 Materials and experimental techniques

In the experiment we have used glass fibers with diameter 8–12 μm, which were made by heating of 125 μm optical glass fibers with oxygen-hydrogen torch and precisely controlled stretching using micrometer translators [41]. After stretching to a desired diameter, the fibers were first cleaned in a solution of water and few percentage of detergent in ultrasonic bath for 30 min. Then the detergent was removed by rinsing with deionized water for several times. In order to remove all organic material from the fibers, they were placed in oxygen plasma (Tegal plasmaline 421) at 100 °C for 1 hour. After cleaning the fibers, their surface was coated with DMOAP silane (*octadecyldimethyl (3-trimethoxysilylpropyl) ammonium chloride*, ABCR GmbH) that ensures strong perpendicular surface anchoring of nematic liquid crystal 5CB [15,16]. The fiber from the tapered end was placed between two parallel optically transparent ITO coated glasses covered with a thin layer of a rubbed polyimide (PI-2555, Nissan Chemicals), which ensure good planar LC orientation. The ITO coating was also used as an absorber of the laser-tweezers light at the surface of the glasses and provided very good control of the local heating of the LC. The gap between glass plates was controlled with mylar spacers and was varied from 16–70 μm. The cell was glued with two component epoxy glue (UHU, GmbH or Torr Seal, Varian). The cell thickness was measured using spectrophotometer (USB2000, Ocean Optics). Then the fiber was cut from the tapered part with a length of 200–600 μm. In all experiments we have used 4′-pentyl-4-cyanobiphenyl (5CB) nematic liquid crystal (Nematel). By filling the cell with the 5CB, the micro-fiber moves inside the cell by capillary force of the LC flow. In the experiments the long axes of the fibers were oriented parallel or perpendicular to the rubbing direction using laser tweezers. In some experiments silica microspheres with 10 μm diameter (Duke Scientific), also treated with silane for perpendicular LC orientation at the surface, were immersed in the same cell.

We have used laser tweezers setup built around an inverted microscope (Nikon Eclipse, TE2000-U) with an infrared fibre laser operating at 1064 nm as a light source and a pair of acousto-optic deflectors driven by computerized system (Aresis, Tweez 70) for trap manipulation. The trajectories of the micro-particles were video recorded using the Pixelink PLA 741 camera at a frame rate of 20 fps. In an off-line analysis, the positions of micro-particles were determined by a video-tracking procedure with a typical resolution of particle's position of $\pm$15 nm.

3 Topology, entanglement and interaction of a microsphere with a micro-fiber parallel to the far-field nematic director

3.1 Creation and manipulation of Saturn rings and anti-rings on a micro-fiber

A micro-fiber (or a micro-rod) is topologically equivalent to a microsphere. In a planar aligned layer of a NLC,

a fiber with a homeotropic (*i.e.* perpendicular) surface alignment of LC molecules is therefore accompanied by a single hyperbolic hedgehog defect, or a Saturn ring, as demonstrated recently [26]. Whether the defect is a point or a ring, depends on the surface anchoring strength and confinement induced by tightly spaced cell. Director field around short fibers with planar surface anchoring has been studied recently in a smectic-A phase by fluorescent confocal polarized microscopy [42]. Interestingly, a fiber is also topologically similar to a capillary, as a capillary can be obtained by performing an inversion operation on a fiber. Topological defects on a fiber will therefore be, to a certain extent, similar to the topological defects in capillaries [43–45].

One can therefore anticipate that an additional homeotropic colloidal particle should bind to the fiber either via the elastic deformation (as any pair of spherical colloidal particles do), or by entanglement of the Saturn ring of the fiber with the Saturn ring of the microsphere. Now, the question emerges whether it is possible to create not only a single Saturn ring on a fiber, but a series of pairs of Saturn ring and anti-ring. Here the Saturn anti-ring is a ring, encircling the fiber (or a sphere), which has a winding number of $+1/2$. Such a ring is not stable individually, but the conservation of the topological charge in principle allows for the simultaneous creation of a pair of a ring and an anti-ring with opposite windings and topological charges.

We have recently demonstrated full control over the creation and stabilization of an arbitrary number of pairs of topological defects on a fibre with opposite topological charges and winding numbers [40]. When a relatively long homeotropic fibre (*i.e.* silanated by DMOAP) of diameter $\sim 10\,\mu$m is inserted into a planar layer of a NLC, and is oriented along the rubbing direction, one can observe a single Saturn ring, encircling it. Far away from this ring, the fiber is defect free, as shown in the first panel of fig. 1(a). By focusing a strong light of the laser tweezers (several 100 mW), the NLC is locally molten in the isotropic phase, creating a tens-of-micrometer-diameter island of the isotropic NLC around the fiber. When the light is switched off, a dense tangle of topological defects is immediately created, following the Kibble-Zurek mechanism of monopole creation in the early Universe [46–48]. During the coarsening time, most of defect mutually annihilates except for a pair of a ring and an anti-ring, as demonstrated in the last panel of fig. 1(a).

The sign of the topological charge of the two rings can be determined by probing the elastic deformation field around the fibre, as opposite topological charges generally attract. As a reference charge, we use a small test particle, treated for perpendicular anchoring, which is by convention assigned a $+1$ charge for the particle and -1 charge for the accompanying Saturn ring. Such a particle induces an elastic distortion that repels the equally charged part of an elastic dipole and attracts the oppositely charged one. The winding number of each ring (and therefore its topological charge) is measured by using a small test quadrupolar colloidal particle, as shown in panels in fig. 1(b). By

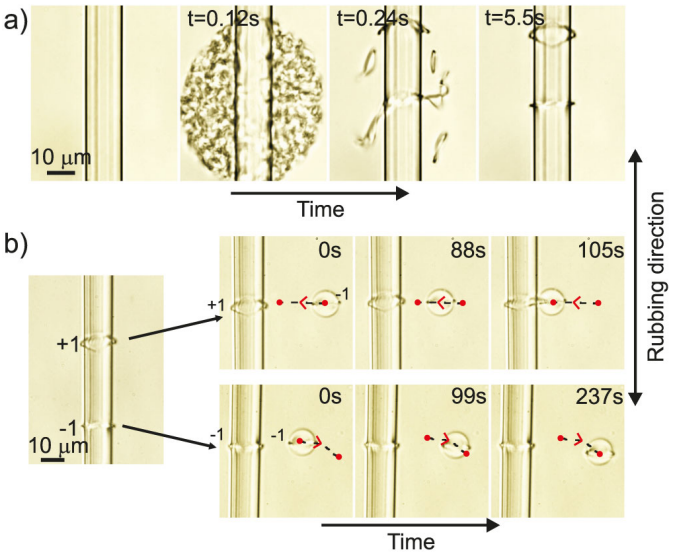

Fig. 1. (a) Controlled creation of a pair of Saturn ring and anti-ring, using a rapid temperature quench of an isotropic island on a micrometer-diameter glass fibre in the NLC 5CB. The isotropic island is created by local heating due to the strong and focused light of the laser tweezers. (b) The winding number of each ring on the fiber is tested using a small quadrupolar microsphere. The Saturn ring of this microsphere has a $-1/2$ winding, which is attracted to the $+1/2$ winding number ring via the elastic forces, and vice versa. It is repelled from the ring with equal winding number, as shown in the bottom series of images.

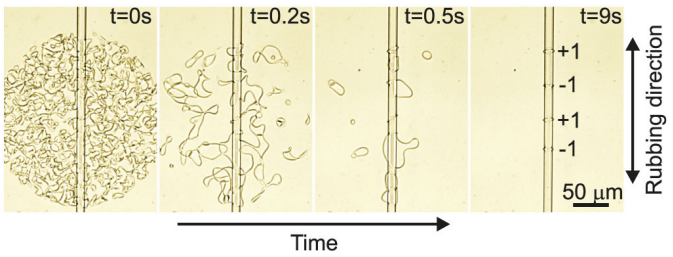

Fig. 2. Using a stronger light of the tweezers creates a larger isotropic island, and two pairs of Saturn ring and anti-ring are created after the quench in this case.

remembering that the winding number of the Saturn ring of this test particle is $-1/2$, one can anticipate that this particle will be attracted to the $+1/2$ ring on the fiber, or repelled from the $-1/2$ ring on the fibre. This is indeed observed in the experiments, as shown in fig. 1(b). For detailed discussion on the topological charge determination see ref. [40].

When the power of the laser tweezers is increased, the diameter of the isotropic island increases as well. Then, after shutting off the light several ring-anti-ring pairs may be created, as shown in fig. 2. We found out that in fact an arbitrary even number of rings with alternating winding numbers can be created and stabilized on the fiber [40].

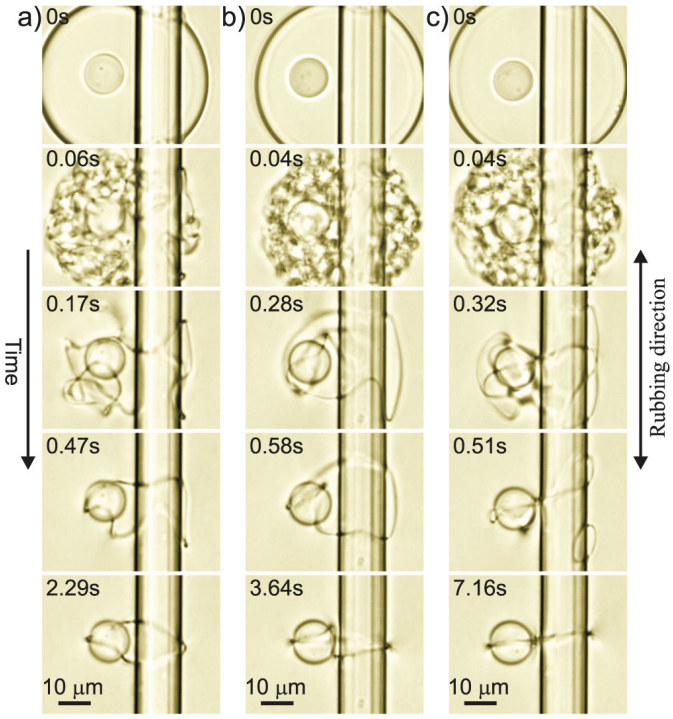

Fig. 3. The entanglement of the $-1/2$ Saturn ring of the fiber with the Saturn ring of a microsphere. Micro-fiber with the diameter of $12\,\mu$m and microsphere with the diameter of $10\,\mu$m are bound together by thermal quench using a focused laser light. (a) Figure of eight is created from one twisted loop. (b) Figure of omega is made from a single loop encircling the colloids with a twist segment between them, which is curved like an additional small loop. (c) An entangled hyperbolic defect is formed from two loops by a direct quench, or by transformation from an unstable figure of omega.

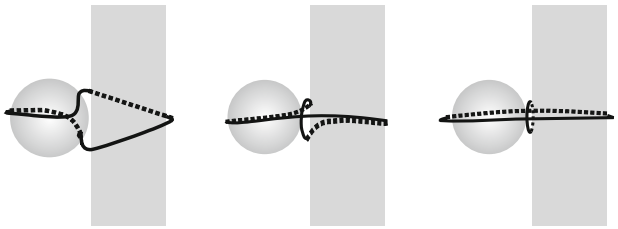

Fig. 4. Schematic representation of the binding of the microsphere to the micro-fiber with Saturn ring. Figure of eight (first panel), figure of omega (second panel), and entangled hyperbolic defect (panel three).

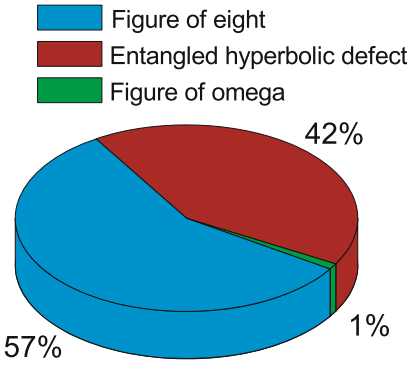

Fig. 5. Probability distribution for the formation of different fiber-sphere entanglement after the temperature quench. In total of 100 experiments, 57 of the final states were figure of eight, 42 of the states were entangled hyperbolic defect and only 1 state was figure of omega.

3.2 Entanglement of a $-1/2$ ring on the micro-fiber and a $-1/2$ ring on the microsphere

In these experiments small spherical colloids with homeotropic surface anchoring and a diameter of $10\,\mu$m are inserted into the 5CB. A single microsphere is guided by the laser tweezer next to the micro-fiber with a pair of Saturn ring and Saturn anti-ring. We have first studied the entanglement between the Saturn ring around the micro-fiber (winding number $-1/2$) and the Saturn ring of the microsphere. By thermally quenching a thin layer of the NLC around the Saturn ring and microsphere, three entangled defect structures have been found, as shown in fig. 3. These entangled structures are identical to the entanglement of two microspheres, which have been predicted by Araki and Tanaka [30] and the Ljubljana group [31] and then observed by the Ljubljana group [32].

We can clearly see three different types of entanglements in fig. 3, which shows the time sequence of unpolarized optical micrographs of the formation of binding between the micro-fiber with $-1/2$ Saturn ring and the $-1/2$ Saturn ring of the microsphere. In fig. 3(a) a single disclination loop is created out of a dense tangle of topological defects after the quench. This loop is encircling the micro-fiber and microsphere in the form of a twisted loop, known as a "figure of eight". Another kind of binding with a single loop is shown in fig. 3(b) and known as a "figure of omega". This entanglement is unstable and may transform into another more stable configuration, which is called "entangled hyperbolic defect" (fig. 3(c)).

In the case of the figure of eight the disclination line first starts from the front of the microsphere and then goes below the fiber and comes from behind over the fiber and again goes down below the microsphere and connects to the first end. This twisted loop looks like a number eight from top view (see fig. 4 first panel). For the figure of omega, the configuration of the loop is more complicated. First a straight defect line passes from the front side of the micro-fiber and microsphere and then goes behind them with an additional loop between them. This middle part of the loop is similar to the Greek letter Ω when observed along the fiber and sphere (fig. 4 second panel).

The entangled hyperbolic defect is formed from two separated defect rings, which are oriented perpendicular to each other. One ring is encircling the micro-fiber and the microsphere and stabilizes the microsphere next to the fiber. The smaller ring, which is placed between the fiber and the sphere, is indeed a -1 hyperbolic point defect with an escaped core (fig. 4 third panel). This type of entanglement can be created in two different ways. First, directly by quenching the NLC around the micro-fiber and micro-

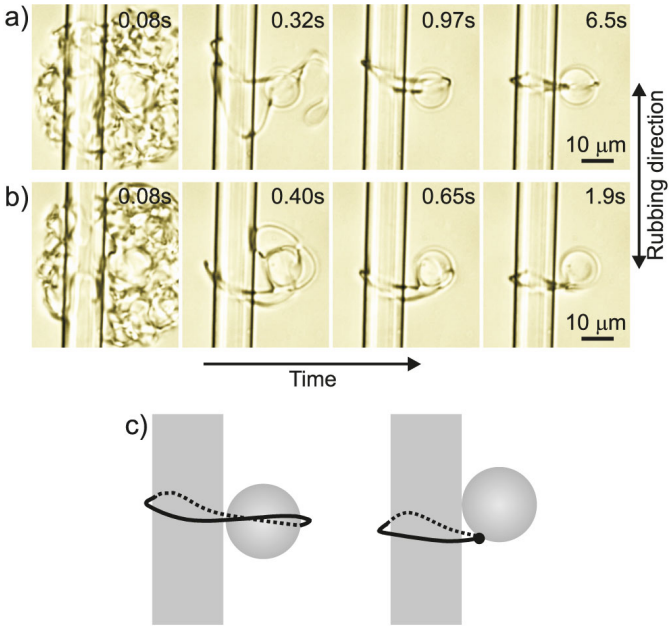

Fig. 6. The entanglement of the $+1/2$ Saturn anti-ring on the micro-fiber with the $-1/2$ Saturn ring on the microsphere. The NLC around micro-fiber (diameter $12\,\mu$m) with a Saturn anti-ring and microsphere (diameter $10\,\mu$m), carrying the Saturn ring, is quenched. Two kinds of entanglement are created. (a) A twisted loop encircling both the fiber and sphere. (b) A sphere loses its Saturn ring, which is attracted towards the fiber and transforms into a -1 hyperbolic point defect. This defect is connected to the Saturn anti-ring on the fiber. (c) Schematic representation of these two entanglements. The left panel shows the binding by a loop and the right panel shows the binding by a point defect.

sphere, and second, via the transformation of the figure of omega to the entangled point defect, as this configuration is more stable.

By repeating the experiments we have found that the probability of creating the figure of eight is significantly higher than the others. The figure of omega is created very rarely, as this configuration is unstable and the defect lines prefer to stabilize in the form of an entangled hyperbolic defect, which is stable. Figure 5 shows the pie chart of the probabilities of different entanglements.

3.3 Entanglement of a $+1/2$ ring on the micro-fiber and a $-1/2$ ring on the microsphere

The entanglement of the $-1/2$ ring on the fiber with the $-1/2$ ring on the colloidal particle is in fact topologically equivalent to the well-known entanglement of two or several microspheres in the nematic liquid crystal, observed in laser tweezers experiments [32]. However, the question is: could one entangle the $-1/2$ ring of the colloidal particle with the $+1/2$ ring on the microfiber? Could this be realized in the experiment?

In order to study the entanglement between the $+1/2$ Saturn anti-ring on the micro-fiber and $-1/2$ Saturn ring on the microsphere, the NLC around the micro-fiber and the microsphere is thermally quenched by the laser beam. Two different kinds of binding are created, as shown in fig. 6(a,b). In fig. 6(a), the time sequence of images shows how a single loop is left out of a dense tangle of topological defects after the quench. This loop is simply encircling the micro-fiber and microsphere with a small twist in the middle sections. The first panel in fig. 6(c) shows the schematic view of it. The disclination line is slightly twisted, it first goes above both the micro-fiber and the microsphere, then sinks below them and reconnects.

The second type of binding of the $+1/2$ and $-1/2$ rings is shown in fig. 6(b). One can clearly see that the $-1/2$ ring of the microsphere has shrunk into a -1 point defect, which is now sitting between the fiber and the sphere and connects the microsphere to the Saturn anti-ring (with positive topological charge) of the micro-fiber. As the point defect of the microsphere and the Saturn anti-ring of the fiber have opposite topological charges, they simply bind together as shown in fig. 6(b) and schematically in the second panel of fig. 6(c).

It is interesting to note that the single ring, entangling the $+1/2$ and $-1/2$ rings, shown in the first panel of fig. 6(c), has to be a charge-neutral ring. This means it has to be composed of a section having $+1/2$ winding, which smoothly transforms into a section with $-1/2$ winding and back. This kind of zero-topological charge loop has in fact been observed recently [40] and its structure was revealed using the Landau-de Gennes numerical modeling.

3.4 Elastic interaction of a dipolar colloidal particle with the fiber

In addition to the mechanism of entanglement, where the fiber and the sphere are linked together by a defect loop, which is formed during a local temperature quench, the usual elastic interaction between the fiber and the microsphere is also observed. In this case, each object (*i.e.* the fiber and the microsphere) has its own localized topological defect either in a form of a ring or point, and is either attracted to or repelled from the other object. This is due to the elastic forces between topologically charged objects and is the result of the inhomogeneous director field due to defects.

Figure 7(a) demonstrates such an elastic interaction between a $11.6\,\mu$m-diameter micro-fiber with a dipolar microsphere (diameter $\sim 10.5\,\mu$m) in a $17\,\mu$m-thick planar nematic cell. The fiber is parallel to the bulk orientation of the nematic liquid crystal with its hyperbolic hedgehog defect on top, *i.e.* far away from the region where the interaction with the microsphere is measured. In this particular experiment in fig. 7 the hyperbolic hedgehog defect of the microsphere is pointing downwards, and the sphere is brought close to the fiber by the laser tweezers and left free by switching off the laser. As shown in fig. 7(a), the interaction between the fiber and dipolar colloidal particle is in this case attractive.

The elastic forces between colloidal particles in nematic LCs can be measured by video-recording the trajectories $r(t)$ of interacting particles. When a pair of col-

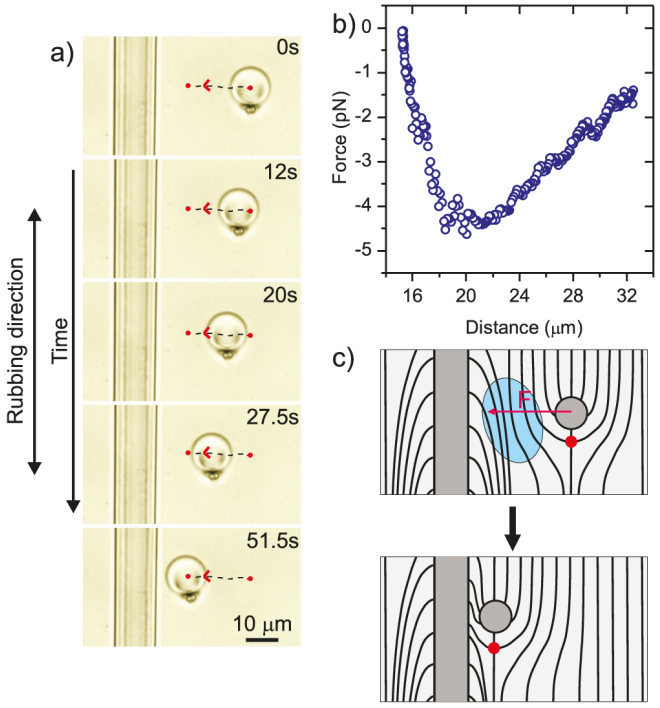

Fig. 7. Attractive interaction between a fiber and a dipolar microsphere. (a) A sequence of optical micro-graphs of the attraction between the fiber and microsphere with opposite directions of their topological dipoles. The point defect of the micro-fiber is out of the field of view, and is situated on the top-side of the fiber (see also the schematic picture). The dashed lines indicate the attractive trajectory. (b) The attractive force *versus* fiber-sphere separation, as extracted from a series of video images. Note that this is center-to-center separation. (c) Schematic representation of the director in the vicinity of the fiber and microsphere. Shaded region denotes elastically distorted liquid crystal, which is in favor of both particles. This generates an attractive elastic force on the microsphere.

loidal particles are brought close to each other by the laser tweezers and left free by switching off the laser, there will be either long-ranged attractive or repulsive force between them, depending on the topology and the geometry of the experiment. The colloidal motion in a fluid of viscosity η experiences a Stokes drag force given by

$$F = 6\pi R\eta v. \tag{1}$$

Here, R is the radius of the sphere, v is the velocity of the sphere, and η is the intrinsic viscosity coefficient of the nematic host, which can be determined from Brownian motion of the particle [49–51]. Instantaneous velocity of the particle is calculated as a time derivative of the trajectory, and together with the known viscosity coefficient, the instantaneous force on the particle can be measured from recorded videoframes.

For the purpose of determining the viscosity coefficients of dipolar and quadrupolar colloidal particles, we have analyzed the data from Brownian motion experiments for several microspheres with normal surface anchoring and the diameter of $\sim 11\,\mu$m in NLC cell with planar alignment and thickness of $30\,\mu$m. Averaging over

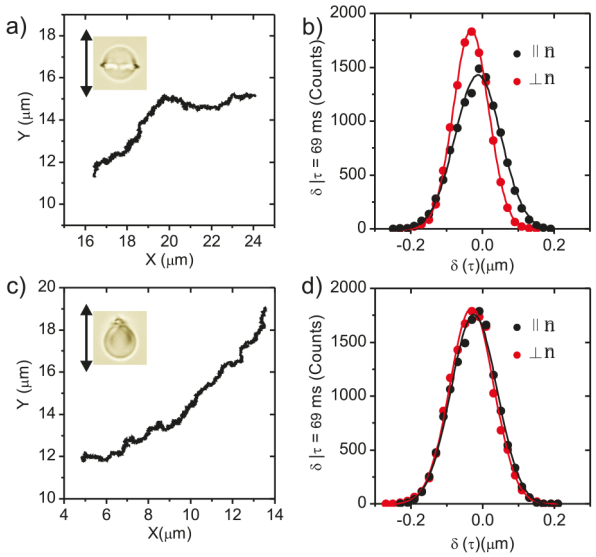

Fig. 8. Brownian trajectories of 9 μm sphere with homeotropic surface anchoring in NLC cell, inducing (a) quadrupolar and (c) dipolar elastic distortion. Histograms of particle displacement parallel (Y) and perpendicular (X) to the director (n) for $\tau = 0.069$ (the time between two consecutive steps) from a sample over 12000 trajectory steps for (b) quadrupolar and (d) dipolar configuration. Because the particles are big and heavy, they exhibit little Brownian motion and the effects of thermal drift and flow of the LC become important, as can be seen from drifting trajectories and the offset of histograms.

12000 steps, the histogram of the particles diffusion with a Saturn ring is shown in fig. 8(a) and with a point defect in fig. 8(c), for both the $x(\perp n)$ and $y(\|n)$ directions with respect to the nematic director. The histograms are fitted to the Gaussian distribution (fig. 8(b) and (d)). From the width of the Gaussian distribution, the self-diffusion coefficient, D, and therefore the viscosity, η, can be calculated for a given particle. For a dipolar colloidal particle we typically obtain $\eta_{\|} = 0.06\,\mathrm{kg/m\,s}$ and $\eta_{\perp} = 0.07\,\mathrm{kg/m\,s}$, whereas for a quadrupolar colloidal particle, both viscosities are slightly higher, $\eta_{\|} = 0.07\,\mathrm{kg/m\,s}$ and $\eta_{\perp} = 0.085\,\mathrm{kg/m\,s}$. This is a typical result [49–51], indicating that colloidal Brownian motion is easier along the nematic director.

The force exerted on the dipole is calculated as a function of the center-to-center separation of the fiber and sphere from $\sim$ 10000 of recorded video frames. The position of the dipole is extracted from the series of images using a video-tracking technique [16]. The value of the viscous-drag coefficient for a dipole is calculated from a separate Brownian motion experiment, and the separation-dependence of the force is derived, as shown in fig. 7(b). The force is attractive and the maximum value is of the order of $\sim 5\,$pN at the center-to-center separation of $\sim 20\,\mu$m, *i.e.* $\sim 7\,\mu$m surface-to-surface separation. Figure 7(c) shows the schematic representation of the director field around fiber and dipole. Because in this case the position of the point defect of the fiber is on the top part of the fiber in fig. 7(a), *i.e.* the opposite to the position of the point defect of the microsphere, the fiber and the sphere

attract. This is similar to the attraction of two antiparallel dipolar colloids, placed side by side to each other [23].

This attractive structural force can be easily understood by considering the schematic drawing of the director field between the fiber and the dipolar particle in fig. 7(c). If we follow the orientation of the director field, as we travel from the fiber to the dipole, the director is first perpendicular to the fiber, then gradually turns clockwise by 90 degrees towards the rubbing direction, and then starts turning counter-clockwise to match the perpendicular alignment at the surface of the colloidal dipole. In total, this is a region of a zero-angle total rotation, which is costing the elastic energy, indicated by the shaded region in fig. 7(c). It can be squeezed out by approaching the microsphere to the fiber. In this case, by putting the dipole closer to the fiber, the director is less twisted, which reduces the energy and the pair-interaction force is therefore attractive.

Alternatively, the structural force between particles in a nematic LC can be understood using the principle of sharing of the field, which is quite common in physics. Namely, each of the particles is surrounded by its own elastically deformed director field. Far away, these regions do not overlap and the structural force is zero. When particles approach each other, the elastically distorted regions start to overlap. If this overlapping region is "in favor" of both particles, they will tend to share it as much as possible. This will generate an attractive force. On the contrary, if the overlapping region is energetically not in favor of both particles, they will repel. One can immediately see from the shaded regions, indicating elastically distorted director field in figs. 7, 9, 10, and 14, whether the particles will attract or repel.

A quite opposite behavior is observed, when the direction of the topological dipole of the microsphere is reversed, as presented in fig. 9. In this case, the position of the point defect of the micro-fiber has been reversed by laser tweezers from downwards (in fig. 7) to upwards direction in fig. 9. One can immediately see in the experiment that the interaction is now repulsive, compared to attractive in previous configuration. The reason for this repulsion is now clearly seen from the director field between the fiber and the sphere. Here, the director turns clockwise by 180 degrees when going from the surface of the fiber to the surface of the microsphere. There is no way to remove this 180 degrees splayed region, and it looks like a domain wall, separating the fiber and sphere. Because the elastic energy, stored in this deformed region is quadratic in the deformation rate, it actually increases when we try to reduce the separation, and the interaction is increasingly repulsive, as shown in fig. 9(b). In the inset to fig. 9(b) we have plotted the repulsive force as a function of center-to center separation of the fiber and sphere. The interaction force shows a power-law behavior, $F(r) \sim r^{-4\pm0.2}$, confirming the dipolar nature of the interaction force. The upper inset shows the schematic view of the director field around the fiber and dipolar colloidal particle, which indicates 180 degrees rotation of the director field between them.

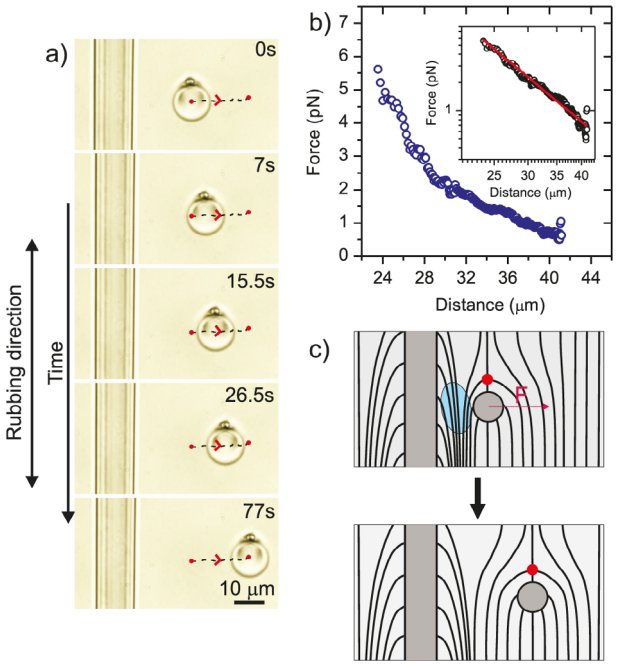

Fig. 9. By reversing the direction of the topological dipole of the microsphere, the interaction between the fiber and microsphere turns from attractive to repulsive. (a) The microsphere is repelled from the fiber when their point defects are pointing into the same direction. The dashed lines show the repulsive trajectory. (b) The repulsive force decreases by increasing the separation. The inset presents the force in a log-log scale with the best fit to a power law with an exponent of -4 ± 0.2. (c) Schematic representation of the director in the vicinity of the fiber and microsphere, showing elastically distorted region in shaded region, which generates repulsion. By increasing the separation between the fiber and the microsphere, the distortion is relaxed and the energy is lowered.

3.5 Elastic interaction of a dipolar or quadrupolar colloidal particle with the rings on the fiber

By quenching the LC around the fiber with laser tweezers, a pair of rings with opposite topological charges can be created encircling the fiber (see sect. 3.1). It is clear that the formation of this pair of charges in general changes the director field in the vicinity of the fiber, as shown in fig. 10 and these changes have a substantial effect on the pair interaction forces between the topological charges on the fiber and those of the particles. The interaction between a fiber with or without rings and the dipolar particle can be understood in terms of topological charges and the repulsion of equally signed charges and attraction of oppositely charged topological defects.

When a pair of rings with opposite topological charge is created on a fiber and the microsphere is positioned between the rings, the +1 ring will attract the −1 charge of the microsphere (*i.e.* the hyperbolic hedgehog accompanying the microsphere) and the −1 ring will attract the body of the microsphere, which has the +1 radial hedgehog hidden in the center of the microsphere. In this constellation,

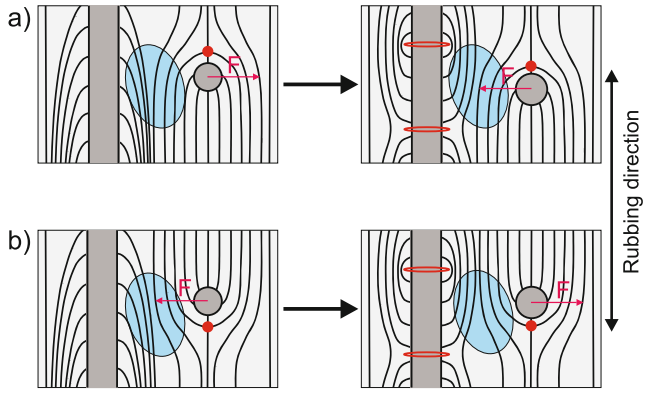

Fig. 10. Schematic representation of the director around the fiber (without and with Saturn ring and Saturn anti-ring) and microsphere. (a) The hyperbolic hedgehog defect is on top of the fiber as well as microsphere. The fiber and microsphere repel each other. The second panel shows the same fiber after creation of the rings. The director between the rings is now changed and the microsphere is attracted to the fiber. (b) The defect of the microsphere has been reversed and is now on the bottom of the sphere. After the rings are created the director between the rings is changed and the interaction is reversed from attraction to repulsion.

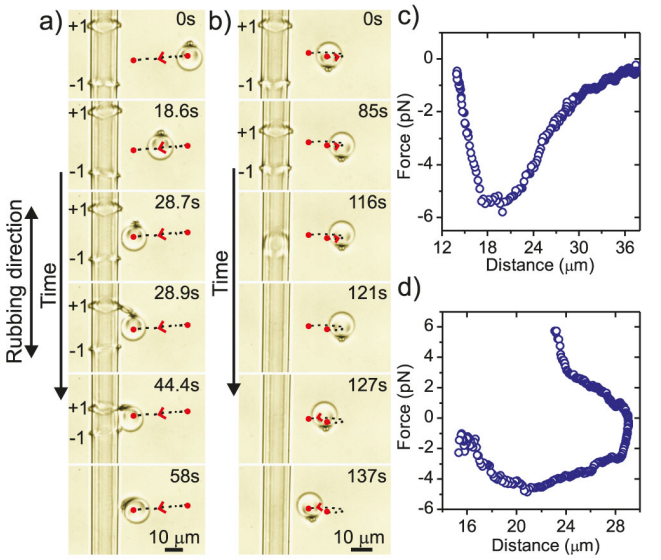

Fig. 11. Interaction between a pair of rings on a fiber with a dipolar microsphere. (a), (b) The dipolar microsphere is either repelled or attracted to the fiber. This depends upon the distribution of the topological charges on the fiber and microsphere. The dashed lines show the trajectory of the dipole after it is released from a position close to the fiber. The red points show the start and end points, the red arrows show the direction of the movement. (c) The attractive force between the fiber and dipole in case (a). (d) The force between the dipole and fiber, which is shown in case (b). First, the force is repulsive, however, after the annihilation of the topological rings on the fiber, the force becomes attractive.

the fiber and the dipolar microsphere will attract each other. If we now reverse the direction of the topological dipole of the microsphere, the interaction should change from attractive to repulsive.

It is exactly this behavior that we observe in the experiments, as shown in the sequence of optical micro-graphs in fig. 11(a), which are extracted from the recorded video. In the first panel we see a dipolar colloidal particle, which is positioned in the middle of a pair of oppositely charged rings and is attracted to the fiber. During this interaction, the rings on the fiber start to move towards each other, as they have opposite topological charges. When the dipole approaches the fiber, the +1 ring is attracted to its − end and the −1 ring is attracted to the + end of the dipole, as shown in the fourth and fifth panel. Then, the two rings annihilate each other and the dipole is starting to be repelled from the fiber (sixth panel). From the recorded video-frames we calculated the position dependence of the attractive force, which is presented in fig. 11(c) *versus* the center-to-center separation. The maximum force is at the separation of 20 μm and is in the order of ~ 6 pN.

When we switch the direction of the dipole and the constellation of the two rings on the fibre remains the same, the interaction force becomes repulsive (see fig. 11 (b), first and second panels). The rings on the fiber individually attract each other because of their opposite topological charges. After the annihilation of the rings, the director field in the vicinity of the fiber is in the same direction as around the microsphere, and the sphere is attracted to the fiber (see fig. 11(b), panels three to six). In this case, the force between the fiber and dipole is shown in fig. 11(d).

In the next experimental setting we replace the dipolar microsphere with a quadrupolar one, carrying a Saturn ring, again with the negative topological charge. As shown in fig. 12(a), the particle is brought close to the Saturn ring of the fiber and released. As both Saturn rings have the same topological charges, the sphere is repelled from and attracted towards the Saturn anti-ring on the fiber. The trajectory of the quadrupolar microsphere is shown in fig. 12(b), and the force between the rings on a fiber and a microsphere is shown in fig. 12(c).

In a final set of experiments, the rings have been separated far away from each other and the interaction between microsphere and a single (either $+1/2$ or $-1/2$) ring has been studied. Six different interactions have been measured:

i) A dipolar microsphere with a hyperbolic hedgehog defect on the bottom is released close to the $-1/2$ Saturn ring on the fiber. The dipole starts to gradually move almost parallel to the bulk orientation of the NLC to the bottom. Then the dipole moves to the fiber without any rotation, and reaches the defect ring from + end (fig. 13(a)). Figure 13(b) shows the schematic configuration of the director in the vicinity of the fiber and dipole, which clearly explains why the dipole first moves to the bottom and then to the ring. The interaction force between the $-1/2$ Saturn ring and microsphere is shown in

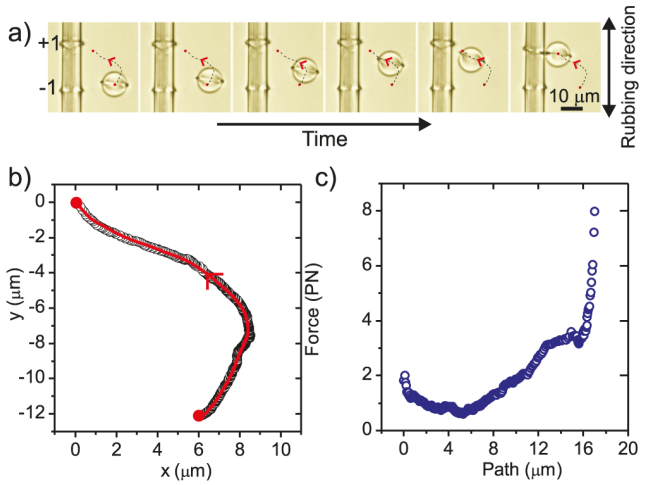

Fig. 12. Interaction of a quadrupolar microsphere with a pair of rings on the fiber. (a) Optical micrographs of the fiber with $+1/2$ and $-1/2$ rings and a quadrupolar microsphere, which demonstrate repulsion of the particle from the $-1/2$ ring and attraction to the $+1/2$ anti-ring. The dashed lines show the trajectories of the quadrupolar microsphere. (b) Trajectory of the quadrupolar microsphere after it was released near the $-1/2$ Saturn ring of the fiber. (c) The interaction force between the quadrupolar microsphere and the rings on the fiber. The microsphere is repelled from the equally charged ring and is attracted to the oppositely charged ring.

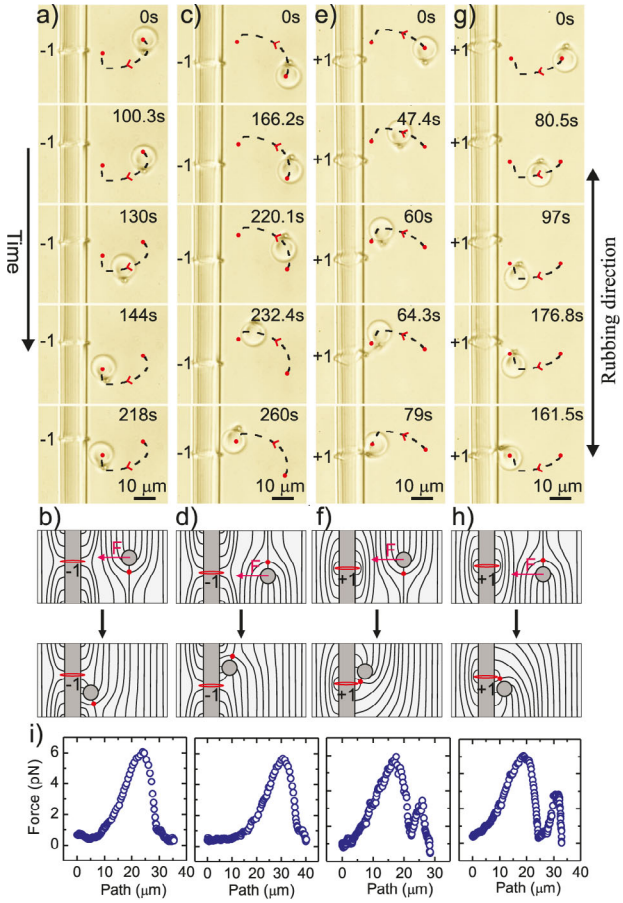

Fig. 13. Interaction of a dipole with Saturn ring or Saturn anti-ring on the fiber. (a,c,e,g) The time sequence of optical micrographs of the attractive interaction between dipole and Saturn ring or Saturn anti-ring. The dashed lines present the trajectory of the dipole. (b,d,f,h) Schematic representation of director around fiber and dipole. (i) The attractive force between dipole and Saturn ring or Saturn anti-ring for panels (a,c,e,g).

fig. 13(i), first panel. The maximum force is of the order of ~ 6 pN.

ii) The hyperbolic hedgehog defect of the dipolar microsphere is on top, and the dipole is released in the vicinity of the $-$ ring of the fiber. First, the dipole moves parallel to the fiber, then, perpendicular to the fiber, as shown in fig. 13(c). Finally, the dipole is attracted to the $-$ ring from the $+$ end. The schematic representation of the director around the fiber and dipole is shown in fig. 13(d). Figure 13(i), second panel, shows the interaction force between the $+$ ring and the dipole.

iii) The dipole with the point defect on the bottom is brought close to the $+$ ring of the fiber and left free (fig. 13(e)). The dipole is attracted to the $+$ ring at a certain angle with respect to the bulk orientation of the NLC. The director around the fiber and dipole is shown schematically in fig. 13(f). The direction of the director in the upper part of the ring is the same as the direction of the director around the dipole. So the dipole stars to move upward and then to the fiber in order to minimize the energy. The interaction force is shown in fig. 13(i), panel three. First, the dipole is attracted to the fiber with the maximum force, approximately equal to 6 pN. In the vicinity of the fiber, the dipole slows down and the attraction force decreases to ~ 1 pN. Then, a rather strong attraction force is applied from the $+$ ring and the dipole is approaching to the ring from its $-$ end (the hyperbolic hedgehog defect). The maximum force is of the order of ~ 4 pN.

iv) The dipole with point defect on top is released close to the $+$ ring of the fiber. It approaches the ring in a nearly semicircular trajectory, as shown in fig. 13(g). Figure 13(h) shows the schematic configuration of the director and fig. 13(i), panel four, shows the interaction force along the path.

v) Figure 14(a) shows the repulsive force between the Saturn ring around the fiber and the microsphere. The schematics is shown in fig. 14(b), the separation dependence of the force is shown in fig. 14(c).

vi) The quadrupolar microsphere is released close to the $+$ ring of the fiber, see fig. 14(d). There will be an attractive interaction between the $-$ charged Saturn ring around microsphere and Saturn anti-ring around the fiber. The quadrupole is attracted to the $+$ ring in the direction perpendicular to the director, and stabilized by the twisted ring, which is encircling the fiber and microsphere, as shown schematically in fig. 14(e). Figure 14(f) shows the attraction force between the fiber and microsphere.

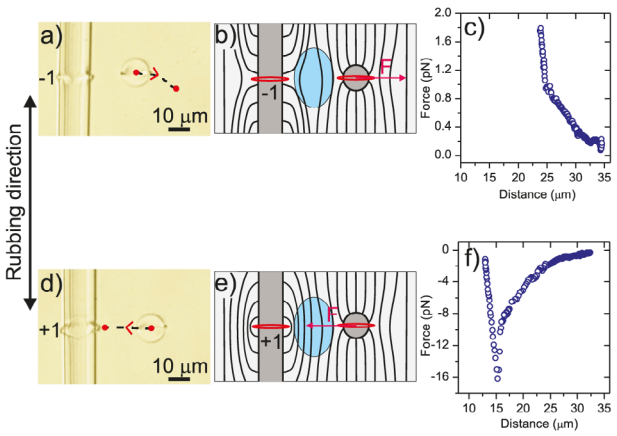

Fig. 14. Interaction of a quadrupole with Saturn ring or Saturn anti-ring on the fiber. (a,b,c) Repulsive interaction between the quadrupole and Saturn ring of the fiber. (d,e,f) Attractive interaction between the quadrupole and Saturn anti-ring on the fiber. The dashed lines show the trajectory of the quadrupole. (b,e) Schematic configuration of director around quadrupole and the topological rings. (c) Repulsive force and (f) attractive force between quadrupole and Saturn ring or Saturn anti-ring, respectively.

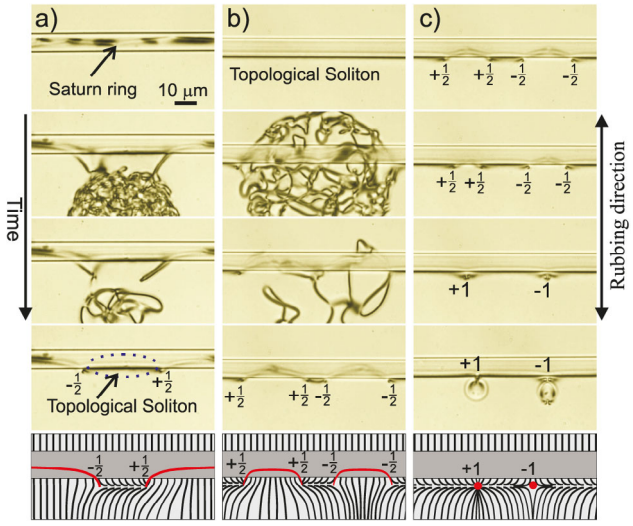

Fig. 15. (a) The micro-fiber is oriented perpendicular to the nematic director in the planar cell, and a gigantic Saturn ring is spontaneously created that encircles the fiber along the long axis. This ring is cut by the laser tweezers into two separated rings with locally opposite winding numbers. The smooth region in between is called "topological soliton". (b) When the region of this smooth topological soliton is quenched, two oppositelly charged loops are created with opposite winding numbers. (c) In the course of time, each of these two loops shrinks into a point defect-a topological monopole, and they have the opposite charges. This is tested by small dipolar colloidal particles. They bind to oppositely charged point defects in opposite orientation of their topological dipole.

4 Topology, interaction and entanglement of a microsphere with a micro-fiber perpendicular to the far-field nematic director

4.1 Topological defects on a fiber

When the fiber is rotated in the nematic liquid crystal to point into a direction, perpendicular to the nematic director, it preserves its Saturn ring, which now appears in a form of a gigantic ring, encircling the fiber all along its length. An example of such a gigantic $-1/2$ ring is shown in the first panel of fig. 15(a). We have recently demonstrated how one can cut and shape individual topological monopoles (defects) out of this gigantic ring by using highly localized and strong beam of the laser tweezers [40]. We briefly discuss here the procedure of obtaining individual topological charges on a fiber, perpendicular to the nematic director, as illustrated in fig. 15.

The panels in fig. 15(a) show how one can cut the $-1/2$ Saturn ring by the laser tweezers in two separate parts. The tweezers is focused at the position, slightly off-the fiber, and by increasing the laser power, the tweezers grabs the ring, and the nematic is locally molten into the isotropic phase. After shutting off the light, a dense tangle of topological defects appears in the region of rapidly cooling nematic (shown in the second panel of fig. 15(a)), which is rapidly coarsening, leaving behind two rings, separated by a region, called the "topological soliton".

Because the starting Saturn ring had a $-1/2$ winding number and the topological charge of -1, this charge has to be distributed between the two new rings. This means that one of the rings must preserve the -1 charge and local $-1/2$ winding, whereas the other ring must be charge-neutral, with $+1/2$ local winding number at the position, facing the $-1/2$ ring (see the last panel of fig. 15(a)).

We can now use the laser tweezers to grab a selected ring and separate the two rings to a larger separation, creating a large region of a topological soliton, shown in the first panel of fig. 15(b). This region has no topological charge, it is only filled with a "topological flux" emanating from one ring and sinking into the other [40]. When the region of topological soliton is quenched, one can see in the third and fourth panel of fig. 15(b) a creation of two loops, sitting on the bottom part of the fiber, where the soliton originally was. In view of the conservation of the topological charge, these two loops must have opposite topological charges, or each of them is a zero-charge loop. If they carry zero topological charge, they should annihilate to vacuum. However, one can see from fig. 15(c) that each of these loops shrinks with time into a point defect, *i.e.* a topological monopole, which has opposite charges. This can indeed be tested by using a test dipolar colloidal particle, which is attracted with its -1 charged hyperbolic defect to the $+1$ monopole and it is attracted with the body of the colloid, carrying the $+1$ radial hedgehog charge to the -1 monopole. It is clear from this experiment that, by repeating the procedure described above, an arbitrary set of alternating topological monopoles can be created on a fiber, oriented perpendicular to the far-field nematic director.

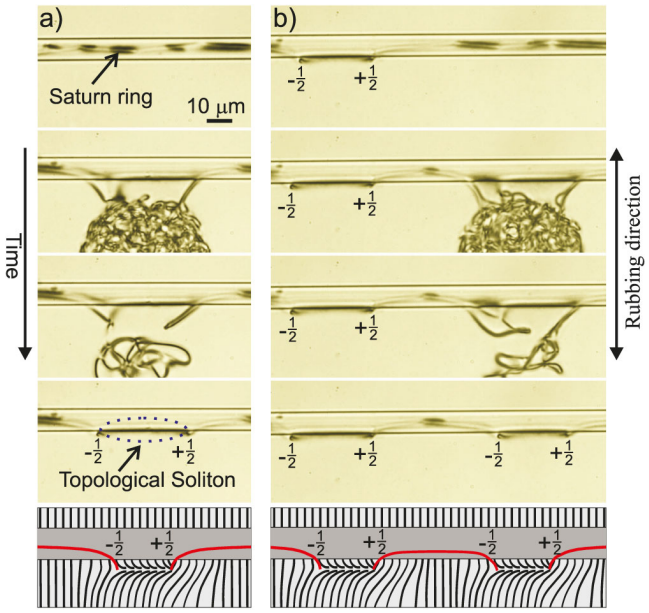

Fig. 16. Creation and structure of a zero-charge loop on a fibre. (a) Such a loop can be created by quenching a topological soliton, which is a smooth region, carrying zero net topological charge. (b) Alternatively, zero-charge loop can be created by quenching a section of $+1/2$ or $-1/2$ loop. There is a certain probability of creating zero-charge loop, which is separated from the remaining defect, in this case $+1/2$ loop.

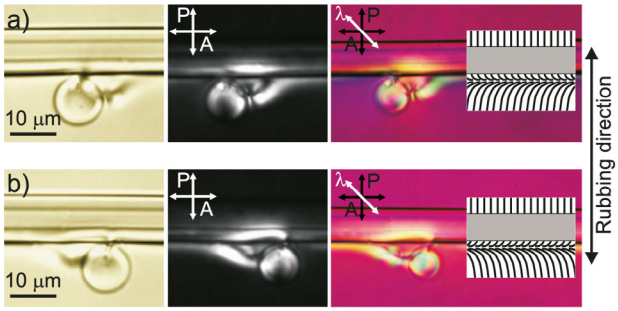

Fig. 17. Interaction of a dipolar microsphere with a topological soliton on the fiber. (a,b) The left images present the unpolarized optical micrographs of a stable orientation of the microsphere, placed within the region of the soliton. The middle images were taken under cross polarizers. The right panels were taken under cross polarizer with a full wave-plate, which is inserted at 45 degrees with respect to polarizer P and crossed analyzer A. The blue and yellow colors clearly show the reversed director field in the vicinity of the fiber in both cases. The schematic drawing of the director field is shown in the insets.

In addition to the alternating set of topological monopoles, we have demonstrated in the same work the existence of charge-neutral loops, attached to the fiber [40]. The loop has zero topological charge, meaning it must be made of a combination of two oppositely charged segments, which transform into each other in two separate places on the loop. As illustrated in fig. 16, this kind of loop can be created in two different ways: i) by quenching the region of a topological soliton, as shown in fig. 16(a). The topological soliton is a region which does not carry any topological charge, therefore objects, which are created out of this region, must carry in total zero topological charge. This can be realized by generating pairs of opposite charges, or by creating, with a certain probability, a zero-charge loop. ii) By quenching a charged loop, as shown in fig. 16(b), there is a certain probability that zero-charge loop will be created on the fiber. Neutrality of zero-charge loops can be verified using a test dipolar colloidal particle, as described in ref. [40].

4.2 Elastic interaction of a microsphere and a fiber

Here we analyze the elastic interaction of a dipolar microsphere with a topological soliton, point defects and zero-charge loops, created on the fiber, as described before. First, a small microsphere with a normal surface anchoring and the diameter of $10\,\mu$m is guided into the vicinity of the fiber with a topological soliton. The stable orientation of the hedgehog point defect of the sphere, carrying the -1 topological charge, is along the topological soliton, which is propagating the topological flux from $-$ charges to the $+$ charges. In other words, the orientation of the topological dipole of the microsphere is such that the -1 part is directed towards the $+$ charge, where the soliton ends. This is clearly presented in figs. 17(a) and (b), where by reversing the direction of the topological soliton, also the stable orientation of the topological dipole is reversed. The configuration of the director field within the soliton can be determined qualitatively by using the λ (red)-plate in both configurations (third panels). The insets to panels present schematic drawings of the director filed.

The interaction force between the fiber with a topological soliton and dipole is studied by bringing a dipolar microsphere into the $\sim 35\,\mu$m separation from the fiber, and releasing it by turning off the laser tweezers. As shown in fig. 18(a), the dipole is attracted to the fiber directly along the director and is rotated at a certain angle for the reduction of the total distortion of the director field. The direction of rotation of the dipole depends on the direction of the topological soliton, which has already been shown in fig. 17. The attractive force *versus* center-to-center separation of the microsphere and fiber is shown in fig. 18(b). The maximum force is of the order of 18 pN at the separation of $17\,\mu$m. If the dipole is rotated by 180 degrees and is released in the vicinity of the topological soliton with its $+$ end facing the soliton, the soliton stars to repel the dipole, as presented in fig. 18(c). The corresponding repulsive force is presented in fig. 18(d).

In the next step, we study the interaction of dipolar microspheres with -1 and $+1$ point monopoles, created on the fiber, as described before. There are two stable configurations of the binding of a dipolar microsphere with -1 point monopole: i) The dipolar microsphere is attracted to the -1 monopole from the $+$ end of the microsphere, as shown in fig. 19(a). ii) It is well known that topological defects with opposite topological charges feel attraction and

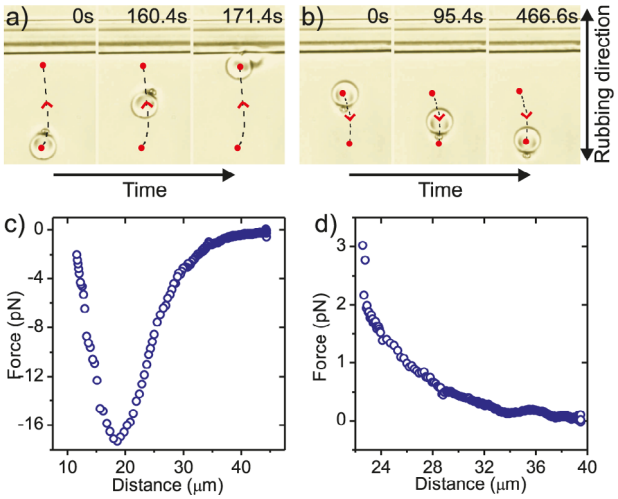

Fig. 18. Interaction between a topological soliton and a dipolar microsphere. (a) The dipole, which is oriented with its − end towards the fiber with a topological soliton, is attracted to the fiber. (b) If the orientation of the dipole is reversed, so that it is facing the soliton with its + end, the particle is repelled from the fiber. (c) and (d) show the attractive force and repulsive force for the experiments (a) and (b), respectively.

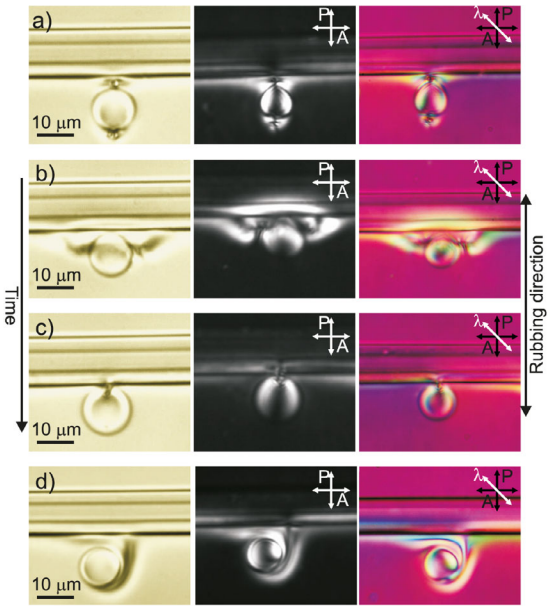

Fig. 19. Binding of a dipolar microsphere with a point monopole on a fiber. (a) Binding of the + end of the dipole with the −1 point monopole on a fiber. (b) Bubble-gum (vortex-like) configuration between the − end of the dipole and the −1 point monopole on a fiber. (c) Stable configuration of the − end of the dipole with the +1 point monopole on the fiber. (d) Binding of the dipole with its + end to the +1 point monopole on the fiber. The first column shows the unpolarized optical micrographs, the second column shows the same image under cross polarizers, and in the third column, the images are taken under cross polarizer and λ wave-plate. The colors enable one to visualize the director field in the vicinity of the dipole and fiber.

with same topological charges feel repulsion arising from the elastic distortion of the NLC in surrounding medium. However, the attractive interaction between like topological charges has been found in LC [2,4,52–54] and is called the "bubble gum", or vortex-like binding. In this mechanism, two point −1 charged hedgehogs fuse together into a non-singular, vortex-like defect structure [54]. In our experiments, a similar exotic defect structure is observed (fig. 19(b)), when the dipolar microsphere approaches to the −1 point monopole from its − end, which is reminding of the bubble gum (vortex-like) structure.

The interaction between the elastic dipole and the +1 point monopole on a fiber also exhibits two different stable configurations. In the first configuration, shown in fig. 19(c), the dipole is attracted to the +1 monopole with the − end of the dipole, which is a typical interaction between two topological defects with opposite topological charges. To obtain the second configuration, we pushed the dipole with its + end towards the +1 monopole by laser tweezers. In this case, shown in fig. 19(d), there is a birefringent, string-like structure between the − end of the dipole and the +1 monopole, similar to a "vortex" around the dipolar microsphere as presented in fig. 19(b). This configuration is very rarely realized in the experiments.

Finally, we study the interaction between a charge-neutral loop and a dipolar microsphere, and two different configurations are considered:

i) The dipole with + end facing the fiber is positioned by the laser tweezers at different separations from the loop and released. The resulting trajectories of the dipole are presented in fig. 20(a). Positions 1, 2, and 3 show the dipole, which is repelled by the topological soliton of the fiber. In the position 4, the dipole is released close to the + end of the zero-charge loop. In this case, the dipole is repelled from the + end and attracted to the − end. In position 5, there is a small repulsion due to the + end of the loop and topological soliton and strong attraction to the − end of the loop. So the dipole is attracted to the − end before it moves far away from the fiber. The positions 6, 7, and 8 are close to the − end of the loop, so the dipole is attracted to the fiber. In positions 9 and 10, there is a repulsive force due to the topological soliton and attraction force due to the − end of the loop.

ii) The dipole is placed at different separations from the loop with its − end facing the fiber. Trajectories of the dipole are shown in fig. 20(b). In the positions 1 and 2, first the dipole is attracted to the topological soliton and then to the + end of the loop. The dipole in positions 3 and 4 is attracted directly to the + end of the loop. In the positions 5 and 6, there is a repulsive interaction between the dipole and the − end of the loop and attractive interaction between the dipole and + end of the loop. When the dipole is placed in positions 7 and 8, there is small repulsive force caused by the − end of the loop and strong attractive force caused by the topological soliton. So the dipole is attracted to the soliton.

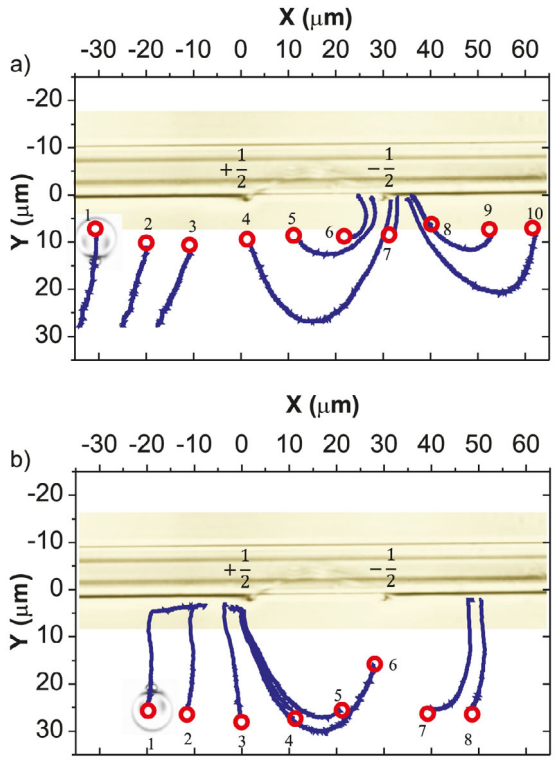

Fig. 20. Trajectories of dipolar colloids in the vicinity of a charge-neutral loop, after it was released from the optical trap towards the fiber. (a) The + end of the dipole is near the fiber. The lines 1-3 show the repulsive trajectories due to the topological soliton close to the charge-neutral loop. The lines 4 and 5 show the dipole trajectories when the particle is repelled by the + end of the loop and topological soliton, and attracted to the − end of the loop. The lines 6-8 show the attractive trajectories towards the − end of the loop. The lines 9 and 10 indicate the trajectories of the dipole with repulsive interaction caused by the topological soliton and attractive interaction caused by the − end of the loop. (b) The − end of the dipole is near to the fiber. The lines 1-4 show the attractive trajectories towards the topological soliton and + end of the loop. The lines 5 and 6 present the repulsive interaction due to the − end of the loop and attractive interaction due to the + end of the loop and topological soliton. The lines 7 and 8 indicate the attractive trajectories towards the topological soliton. Open circles indicate the starting positions.

4.3 Entanglement and binding of a microsphere with far segments of a loop on a fiber

Here we present our experiments of the entanglement and interaction of a microsphere with the far segments of the loops, created on a fiber by cutting the original gigantic Saturn ring. As mentioned before, these segments have a local winding number $-1/2$ or $+1/2$, which can be determined from the optical analysis of images. The results of the experiments are presented in fig. 21.

In the first set of experiments, shown in fig. 21(a-d), a micro sphere is exposed towards the − end of the loop. By quenching the NLC around the − end of the loop and

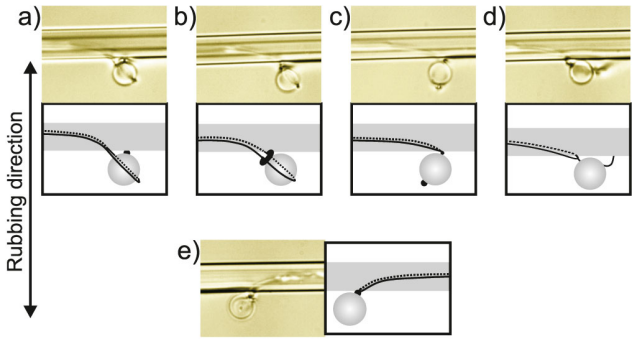

Fig. 21. Entanglement and binding of a microsphere with halves of the charged loop. The panels show the optical images in unpolarized light and the accompanying panels show the schematics. (a) The − end of the loop of the fiber embraces the microsphere. The hedgehog point defect of the microsphere is still there and is attached to the fiber. (b) The − end of the loop is encircling the microsphere and an additional smaller loop, originating from the point hedgehog, is encircling this part of the fiber's loop. (c) In a reversed orientation of the microsphere's hedgehog, the microsphere is now bound to the − end of the loop from its + end. (d) This binding between the − end of the loop and hedgehog point defect is similar to the bubble-gum configuration. (e) The microsphere is bound to the + end of the loop with its − point defect.

the microsphere, four different kinds of binding or entanglement are created, which are shown in fig. 21(a-d). The upper panels show the true microscope images of these bindings under unpolarized light, and the bottom panels show the schematic representation of them.

In fig. 21(a) the end of the loop encircles the dipolar microsphere, and the hedgehog point defect of the particle is located on the top-end of the microsphere and is attracted towards the fiber. Figure 21(b) presents another kind of binding, which is similar to the hyperbolic defect entanglement, observed between two mutually entangled microspheres with Saturn rings in planar cells [32]. In this case the microsphere is bound to the fiber with the end of the loop, and there is a smaller ring between the fiber and sphere.

The microsphere can also be attached to the end of the loop from its + end, as shown in fig. 21(c), or from the − end, as shown in fig. 21(d). In this case we obtain a binding that resembles the bubble-gum binding.

Finally, we can observe the interaction of the microsphere with the + end of the loop, with the $+1/2$ winding environment. There is only one kind of binding between the sphere and fiber, as we can see in fig. 21(e). The microsphere is attached to the + end of the loop with the hedgehog point defect.

5 Conclusions

This work demonstrates detailed analysis of topological properties and interactions of a pair of simple particles, *i.e.* a long micro-fiber and a microsphere, immersed in a homogeneous nematic liquid crystal. We can see from

this simple experimental setting with only two topologically simple objects (*i.e.* both having genus $g = 0$) an amazing diversity of topological states and possible pair interactions. The advantage of this simple experimental setting is that it provides a step-by-step systematic analysis of topological phenomena. We observe in the experiments that the magnitude of elastic forces between the fiber and the colloidal particle are quite similar to what has been observed before when measuring the pair interaction of spherical micro-particles, which is indeed expected. However, we observe new topological phenomena, such as the interaction and entanglement of topological defects on the microsphere with those on the fiber. Here, we use a recently discovered method of producing an arbitrary number of pairs of oppositely charged Saturn ring and the Saturn anti-ring on the fiber and even more exotic production of monopoles and zero-charge loops on a fiber, set perpendicular to the overall nematic orientation in the measuring cell. We find a variety of specific pair interaction, which can be explained using a simple topological rule: like topological charges repel each other and opposite topological charges attract each other. When we use the laser tweezers to fuse and entangle defect loops on the fiber and the microsphere, we not only obtain entangled states observed for spherical colloids, but also exotic entanglement of half-winding number defect loops with equal or opposite winding, or even fusion of half-winding lines with point defects, etc.

Our experiments illuminate recent theoretical analysis of the topology of nematic braids [55]. As mentioned many times before, topological defects with winding numbers $+1/2$ and $-1/2$ are, strictly speaking, topologically indistinguishable, as they can be smoothly transformed into each other by applying a proper local rotation on the director field at each point of the space considered. Interestingly, this hypothetical local rotation, which is used in an abstract topological analysis, is realized in our system on charge-neutral defect loops and in cases where we have entanglement of positive and negative winding number loops. These loops have two parts with opposite winding numbers that are smoothly transformed into each other as we travel along the loop. We have shown that the winding number of these sections can be tested in our system by using small test colloidal particles with known topological charges.

Finally, our analysis of topological binding of fibers and spheres in a nematic liquid crystal definitely opens new routes to very complex colloidal assembly for practical applications in photonics [33, 56]. The experiments also open an interesting question of how the chirality of liquid crystal matrix influences observed topological phenomena. This will be reported in a subsequent publication.

This work was supported by the European Commission Marie Curie project HIERARCHY grant PITN-GA-2008-215851 (M.N.), the Slovenian Research Agency (ARRS) contracts P1-0099, J1-6723 and J1-3612 (I.M., M.Š), and in part by the Center of excellence NAMASTE (I.M.).

Author contribution statement

M.N. performed the experiments and analysis, M.Š. supervised the experiments. I.M. initiated the experiments and supervised the work, M.N. and I.M. wrote the manuscript.

References

1. H. Stark, Phys. Rep. **351**, 387 (2001).
2. T.C. Lubensky, D. Pettey, N. Currier, H. Strak, Phys. Rev. E **57**, 610 (1998).
3. P. Poulin, Curr. Opin. Colloids Interface Sci. **4**, 66 (1999).
4. P. Poulin, D.A. Weitz, Phys. Rev. E **57**, 626 (1998).
5. E.M. Terentjev, Phys. Rev. E **51**, 1330 (1995).
6. R. Pratibha, N.V. Madhusudana, Mol. Cryst. Liq. Cryst. **198**, 215 (1991).
7. O. Mondain-Monval, J.C. Dedieu, T. Gulik-Krzywicki, P. Poulin, Eur. Phys. J. B **12**, 167 (1999).
8. Y. Gu, N.L. Abbott, Phys. Rev. Lett. **85**, 4719 (2000).
9. W.B. Russel, D.A. Saville, W.R. Schowalter, *Colloidal Dispersions* (Cambridge University Press, Cambridge, 1989).
10. J.N. Israelachvili, *Intermolecular and Surface Forces* (Academic Press, London, 1992).
11. P. Poulin, H. Stark, T.C. Lubensky, D.A. Weitz, Science **275**, 1770 (1997).
12. J.C. Loudet, P. Poulin, P. Barois, Europhys. Lett. **54**, 175 (2001).
13. J.C. Loudet, P. Barois, P. Poulin, Nature **407**, 611 (2000).
14. K. Kita, M. Ichikawa, Y. Kimura, Phys. Rev. E **77**, 041702 (2008).
15. M. Škarabot, M. Ravnik, S. Žumer, U. Tkalec, I. Poberaj, D. Babič, N. Osterman, I. Muševič, Phys. Rev. E **76**, 051406 (2007).
16. M. Škarabot, M. Ravnik, S. Žumer, U. Tkalec, I. Poberaj, D. Babič, N. Osterman, I. Muševič, Phys. Rev. E **77**, 031705 (2008).
17. M. Zapotocky, L. Ramos, P. Poulin, T.C. Lubensky, D.A. Weitz, Science **283**, 209 (1999).
18. V.G. Nazarenko, A.B. Nych, B.I. Lev, Phys. Rev. Lett. **87**, 075504 (2001).
19. I. Muševič, M. Škarabot, U. Tkalec, M. Ravnik, S. Žumer, Science **313**, 954 (2006).
20. A.B. Nych, U.M. Ognysta, V.M. Pergamenshchik, B.I. Lev, V.G. Nazarenko, I. Muševič, M. Škarabot, O.D. Lavrentovich, Phys. Rev. Lett. **98**, 057801 (2007).
21. I. Muševič, M. Škarabot, Soft Matter **4**, 195 (2008).
22. U. Ognysta, A. Nych, V. Nazarenko, I. Muševič, M. Škarabot, M. Ravnik, S. Žumer, I. Poberaj, D. Babič, Phys. Rev. Lett. **100**, 17803 (2008).
23. M. Škarabot, I. Muševič, Soft Matter **6**, 5476 (2010).
24. M. Humar, M. Škarabot, M. Ravnik, S. Žumer, I. Poberaj, D. Babič, I. Muševič, Eur. Phys. J. E **27**, 73 (2008).
25. A. Nych, U. Ognysta, M. Škarabot, M. Ravnik, S. Žumer, I. Muševič, Nat. Commun. **4**, 1489 (2013).
26. U. Tkalec, M. Škarabot, I. Muševič, Soft matter **4**, 2402 (2008).
27. S.P. Meeker, W.C.K. Poon, J. Crain, E.M. Terentjev, Phys. Rev. E **61**, 0417021 (2000).
28. V.J. Anderson, E.M. Terentjev, S.P. Meeker, J. Crain, W.C.K. Poon, Eur. Phys. J. E **4**, 11 (2001).
29. V.J. Anderson, E.M. Terentjev, Eur. Phys. J. E **4**, 21 (2001).

30. T. Araki, H. Tanaka, Phys. Rev. Lett. **97**, 127801 (2006).
31. S. Žumer, *Plenary Talk at the 21st International Liquid Crystal Conference, Keystone, Colorado, July 2-7, 2006.*
32. M. Ravnik, M. Škarabot, S. Žumer, U. Tkalec, I. Poberaj, D. Babič, N. Osterman, I. Muševič, Phys. Rev. Lett. **99**, 247801 (2007).
33. I. Muševič, Liq. Cryst. **41**, 418 (2013).
34. M. Humar, I. Muševič, Opt. Express **18**, 26995 (2010).
35. K. Peddireddy, V.S.R. Jampani, S. Thutupalli, S. Herminghaus, C. Bahr, I. Muševič, Opt. Express **23**, 30233 (2013).
36. V.S.R. Jampani, M. Škarabot, H. Takezoe, I. Muševič, S. Dhara, Opt. Express **21**, 20506 (2013).
37. M. Humar, M. Ravnik, S. Pajk, I. Muševič, Nat. Photon. **3**, 595 (2009).
38. M. Humar, I. Muševič, Opt. Express **21**, 19836 (2011).
39. O.D. Lavrentovich, Liq. Cryst. **24**, 117 (1998).
40. M. Nikkhou, M. Škarabot, S. Čopar, M. Ravnik, S. Žumer, I. Muševič, Nat. Phys. **11**, 183 (2015).
41. C.L. Linslal, P.M.S. Mohan, A. Halder, T.K. Gangopadhyay, *Third International Conference on Sensors and Related Networks (SENNET-12)*, VIT University, Vellore, India, Jan. 19-21 (2012) pp. 18–21.
42. G. Liao, I.I. Smalyukh, J.R. Kelly, O.D. Lavrentovich, A. Jákli, Phys. Rev. E **72**, 031704 (2005).
43. P. Kossyrev, M. Ravnik, S.Žumer, Phys. Rev. Lett. **96**, 048301 (2006).
44. V.K. Pershin, I.I. Klebanov, P.B. Zalmanov, Tech. Phys. **44**, 763 (1999).
45. M. Svetec, M. Slavinec, J. Chem. Phys. **128**, 084704 (2008).
46. W.H. Zurek, Phys. Rep. **276**, 177 (1996).
47. B. van Heck, M. Burrello, A. Yacoby, A.R. Akhmerov, Phys. Rev. Lett. **110**, 086803 (2013).
48. I. Chuang, R. Durrer, N. Turok, B. Yurke, Science **251**, 1336 (1991).
49. J.C. Loudet, P. Hanusse, P. Poulin, Science **306**, 1525 (2004).
50. I. Lazo, O.D. Lavrentovich, Philos. Trans. R. Soc. A **371**, 20120255 (2013).
51. T. Turiv, I. Lazo, A. Brodin, B.I. Lev, V. Reiffenrath, V.G. Nazarenko, O.D. Lavrentovich, Science **342**, 1351 (2013).
52. P. Poulin, V. Cabuil, D.A. Weitz, Phys. Rev. Lett. **79**, 4862 (1997).
53. J. Fukuda, H. Yokoyama, Phys. Rev. Lett. **94**, 148301 (2005).
54. U. Tkalec, M. Ravnik, S. Žumer, I. Muševič, Phys. Rev. Lett. **103**, 127801 (2009).
55. S. Čopar, Phys. Rep. **538**, 1 (2014).
56. I. Muševič, Philos. Trans. R. Soc. A **371**, 20120266 (2013).